Terahertz-pulse driven modulation of electronic spectra: Modeling electron-phonon coupling in charge-transfer crystals

Francesco Di Maiolo, Matteo Masino, and Anna Painelli*

Department of Chemistry, Life Science and Environmental Sustainability, Università di Parma, 43124 Parma, Italy

(Received 19 May 2017; revised manuscript received 15 July 2017; published 7 August 2017)

We calculate the optical spectra of a charge-transfer crystal modulated by a terahertz pulse, accounting for electron-vibration coupling. The model Hamiltonian is parametrized against first principle calculations and adiabatic results are validated against a fully non-adiabatic calculation where relaxation phenomena are introduced via the coupling of the quantum system to a dissipative bath of classic anharmonic oscillators. The experiment is well reproduced by the proposed model with no need to introduce any ad hoc assumption on the temporal dependence of model parameters, but just accounting for the quadratic dependence of the Hubbard U on non-totally symmetric molecular coordinates.

DOI: 10.1103/PhysRevB.96.075106

I. INTRODUCTION

Delocalized electrons in reduced dimensions are responsible for the complex and intriguing physics of charge-transfer (CT) crystals [1–3]. The variegated properties of these materials, their complex phase diagrams [4–8] and their unique spectral features [9–11] are governed by a subtle interplay of electron-electron and electron-phonon interactions. In recent years the development of multiple ultrashort pulse techniques made it possible to artificially modulate the material properties following the subsequent dynamics in real time [12,13]. In this respect, the coupling of electronic and vibrational degrees of freedom is a key player. The analysis of coherent oscillations following ultrafast electronic photoexcitation is a well-established tool in molecular physics to investigate excited state potential energy surfaces [14,15] and, in the realm of CT crystals, offered a clear demonstration of anharmonic interactions driven by electron-phonon coupling in the close proximity of photoinduced phase transitions [16–18]. Recent technological advances in the production of well-controlled pulses in the terahertz (THz) and mid-infrared (MIR) [19–22] regions allow to directly address the modulation of basic interactions by specific molecular vibrations or lattice modes, monitoring their spectroscopic effects on electronic excitations [23,24]. These techniques offer an invaluable tool to experimentally validate model Hamiltonians traditionally used to describe coupled electronic and vibrational motion in CT crystals. To fully exploit the potential of these advanced spectroscopic techniques it is important to develop general, reliable and accurate theoretical interpretative tools to describe the coupled electronic and vibrational motion of a system driven out of equilibrium by a specifically designed pulse in the MIR or THz regions.

In this paper we present a comprehensive theoretical description of a recent experiment by Kaiser and coworkers [25,26]. The investigated material, bis-(ethylendithyo)-tetrathiafulvalene difluorotetracyano-quinodimethane (ET-F_2TCNQ), is an organic CT crystal characterized by segregated stacks of ET molecules bearing a positive charge (half-filling) and regularly spaced, as shown in Fig. 1 [27]. The relevant physics is therefore governed by electrons delocalized in one dimension, along the stack of ET^+ molecular ions. A strong pump pulse in the MIR region (900–1100 cm^{-1}), polarized perpendicularly to the stack, selectively drives IR-active (i.e., non-total symmetric) molecular vibrations of ET^+ ions out of equilibrium. A second weaker ultrafast probe-pulse interrogates the system in the NIR (4000–7000 cm^{-1}) region, as relevant to CT excitations, observing coherent spectral oscillations at twice the frequency of the driven molecular mode. We rely on quantum cell models for the description of the coupled electronic and vibrational system, parametrized against quantum chemical calculations. Numerical integration techniques are adopted to explore the dynamics of the driven system, comparing results obtained via a truly non-adiabatic description of the coupled electronic-vibrational motion with the adiabatic solution.

In the next section, we introduce the model and its parametrization. In Sec. III the model is put in action on

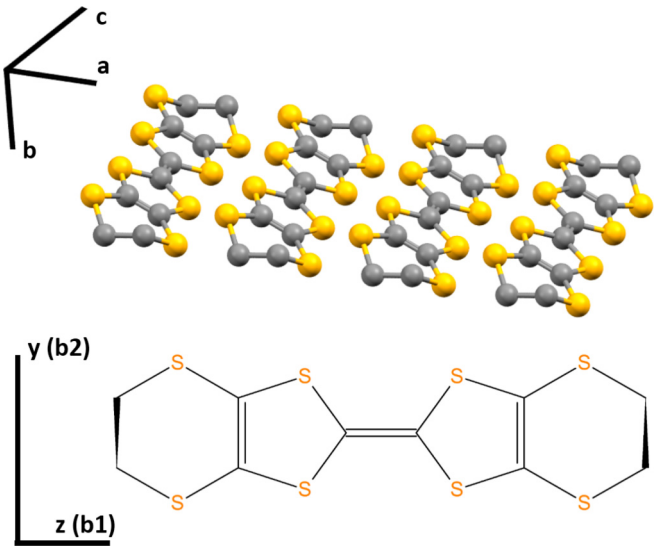

FIG. 1. Top: the ET^+ stack, from crystallographic data in Ref. [27]. Bottom: the chemical structure of ET molecule, the labels along the axis refer to relevant irreducible representations in the D_2 point group.

*anna.painelli@unipr.it

an $(ET^+)_2$ dimer where a fully non-adiabatic approach is adopted. In Sec. IV we compare the non-adiabatic results with those obtained in the adiabatic approximation. Results are summarized and discussed in Sec. V.

II. SETTING THE STAGE: DEFINITION OF THE MODEL HAMILTONIAN

The electronic structure of segregated regular stack systems, like ET-F_2TCNQ, is well captured by the extended Hubbard model:

$$\hat{H}_{el} = -t \sum_{i,\sigma} (\hat{c}^{\dagger}_{i,\sigma} \hat{c}_{i+1,\sigma} + \text{H.c.}) + U \sum_i \hat{n}_{i,\uparrow} \hat{n}_{i,\downarrow} + V \sum_i \hat{\rho}_i \hat{\rho}_{i+1}, \quad (1)$$

where $\hat{c}^{\dagger}_{i,\sigma}$ and $\hat{c}_{i,\sigma}$ are the creation and annihilation operators for an electron with spin σ on site i, $\hat{n}_{i,\sigma} = \hat{c}^{\dagger}_{i,\sigma} \hat{c}_{i,\sigma}$ counts the number of electrons having σ spin on site i, and $\hat{\rho}_i = 2 - \hat{n}_i$ is the ET ionicity operator. The first term in the Hubbard Hamiltonian accounts for the electronic delocalization, with t describing the nearest neighbor hopping. The second term describes the repulsion of two electrons on the same site, U, and the third term accounts for intersite electrostatic repulsions reduced to nearest neighbor interactions, V.

The Hubbard model only accounts for intermolecular electronic degrees of freedom, collapsing the molecular complexity to a single site. This common approximation is justified by the different energy scales of relevant excitations: the lowest localized excitation in ET^+ ions are found at 13 000 cm^{-1}, [28] approximately 0.9 eV higher than intermolecular CT excitation described by the Hubbard model for the system at hand. The molecular complexity is at least in part accounted for assigning internal vibrational degrees of freedom to the molecular sites, able to modify on-site properties, in the spirit of the Holstein model.

Electronic model parameters for ET-F_2TCNQ have already been estimated [25,26,29]. The current estimate $t = 0.04$ eV, is in line with our estimate from ZINDO calculations on $(ET^+)_2$ dimers in crystallographic geometry [30]. U can be estimated from single molecule calculations as [31]

$$U = \mathcal{E}(\text{ET}) - 2\mathcal{E}(\text{ET}^+) + \mathcal{E}(\text{ET}^{2+}), \quad (2)$$

where $\mathcal{E}$ is the ground state energy of the ET molecule in the different oxidation states. Density functional theory (DFT) results (UB3LYP functional, 6-31G(d) basis set, gas phase geometry, using GAUSSIAN09 package [32]) lead to $U = 4.06$ eV, in good agreement with previous estimate [31,33]. The extended Hubbard model in Eq. (1) is an effective model where all intermolecular interactions are collapsed into an effective nearest neighbor V interaction. Accordingly, the actual value of V is difficult to estimate from quantum chemical calculations and is best fixed against experiment. For a dimeric system, to be discussed in Secs. III and IV, only $U - V$ enters the Hamiltonian matrix and we fix $U - V = 0.666$ eV to reproduce the experimental frequency of the CT transition, $\hbar\omega \simeq 0.68$ eV.

In the pump-probe experiment described in Refs. [25,26], IR-active molecular vibrations of ET^+ are selectively excited by an intense pump beam at 1000 cm^{-1} polarized perpendicularly to the stack axis (i.e., perpendicularly to the a crystallographic direction). The optical pulse excites the in-phase motion of the molecules along the stack (the zone-center mode). In these conditions only on-site energies may be sizably affected, but the in-phase modulation of the site energy is irrelevant to the model (the total number of electrons in the stack being constant) so that, as originally suggested in Refs. [25,26], the only relevant modulation involves the Hubbard U (as a matter of fact V modulations are also possible, but they are negligible, see Supplemental Material [34]). IR-active vibrations belong to the irreducible representations b_1,b_2, and b_3 in the D_2 molecular symmetry [35] and, being non-totally symmetric, they can only modulate U quadratically.

TABLE I. Selected results on vibrational modes of ET^+ as obtained from DFT calculations in gas phase. Only IR-active modes in the 900–1100 cm^{-1} spectral region are shown. For each mode, we list the calculated frequency, the β coupling constant, the squared derivative of the molecular dipole moment on the vibrational mode η^2, the squared cosine of the angle between the molecular axis relevant to each vibration with the b and c crystallographic axis.

mode (symmetry)	ω_v cm^{-1}	β meV	η^2 $(D/Å)^2 amu^{-1}$	T_b	T_c
40 (b2)	902	5.4	0.2281	0.28	0.07
41 (b3)	918	-0.5	0.1611	0.72	0.01
42 (b2)	927	1.0	0.0173	0.28	0.07
43 (b1)	958	-0.6	0.2974	0.0	0.90
45 (b1)	1028	0.2	0.1634	0.0	0.90
47 (b3)	1028	-2.2	0.0017	0.72	0.01
48 (b2)	1031	-3.0	0.7663	0.28	0.07
49 (b3)	1063	4.1	0.0060	0.72	0.01

To evaluate the strength of the coupling we resort again to DFT calculations. After geometry optimization of ET^+ in the gas phase [UB3LYP functional, 6-31G(d) basis set], we calculate molecular vibrational modes. Selected results for the 900–1100 cm^{-1} region are reported in Table I, complete results can be found in the Supplemental Material [34]. Vibrational frequencies ω_v are rescaled according to Ref. [35]. The quadratic coupling constants are calculated as

$$\beta_\alpha = \left.\frac{\partial^2 U}{\partial {Q_\alpha}^2}\right|_0 = \frac{U(Q_\alpha) + U(-Q_\alpha) - 2U(0)}{Q_\alpha^2}, \quad (3)$$

where Q_α is the dimensionless normal coordinate associated to the α-th molecular mode and $U(Q_\alpha)$ is calculated according to Eq. (2) for the distorted geometry.

For the sake of simplicity we will account for a single coupled mode, on each molecular site i (the α index will be removed, accordingly). The Hamiltonian reads

$$\hat{H} = \hat{H}_{el} + \frac{\hbar\omega_v}{4} \sum_i \left(\hat{P}_i^2 + \hat{Q}_i^2\right) + \beta \sum_i \hat{Q}_i^2 \hat{n}_{i,\uparrow} \hat{n}_{i,\downarrow}, \quad (4)$$

where ω_v is the frequency of the mode, $\hat{Q}_i$ and $\hat{P}_i$ are the dimensionless vibrational coordinate and its conjugated momentum, of site i. Specifically $\hat{Q}_i = (\hat{a}_i^{\dagger} + \hat{a}_i)$ and $\hat{P}_i =$

$i(\hat{a}_i^\dagger - \hat{a}_i)$ where $\hat{a}_i^\dagger$ and $\hat{a}_i$ are the creation and annihilation operators for the harmonic oscillator.

To discuss optical spectra we must define the dipole moment operators. CT spectra are addressed by the probe-beam in the near-IR region polarized along the stack axis, a. The corresponding dipole moment operator (in units with the electronic charge and the lattice constant set to 1) is

$$\hat{\mu}_a = \sum_i i\hat{n}_i. \tag{5}$$

The pump beam in the mid-IR region forces the oscillation of molecular vibrations. Accordingly, the relevant dipole moment operator is

$$\hat{\mu}_{IR} = \eta \sum_i \hat{Q}_i, \tag{6}$$

where η is the derivative of the molecular ground state dipole moment on the molecular coordinate. The squared η values, calculated for the isolated molecules, listed in Table I, are proportional to the infrared intensity of vibrational modes. While we account for a single vibrational mode in our Hamiltonian, the derivatives of the molecular dipole moment on the vibrational coordinates are calculated for all molecular vibrations, as listed in Table I (see also the Supplemental Material [34]). Based on the relative IR intensities of the vibrational modes and on the director cosines (last two columns in Table I), we expect that the pump beam, perpendicularly polarized with respect to a, will mainly excite the mode number 48. In the following we set $\omega_v = 1031$ cm^{-1}, $\beta = -3$ meV, as relevant to mode 48.

III. NON-ADIABATIC RESULTS

We attack the problem considering the smallest possible stack fragment, i.e., an $(ET^+)_2$ dimer. Indeed the very small t value characterizing ET-F_2TCNQ suggests a strongly localized electron system, as to make a dimer calculation relevant. Thanks to this minimal choice we are able to adopt a fully non-adiabatic approach to the dynamics. Only singlet states are relevant to optical spectroscopy, so that the electronic basis states for the ET^+ dimer are just three: $|\frown\rangle$, $|x0\rangle$, and $|0x\rangle$, where x marks a doubly occupied ET site, 0 an empty ET^{2+} site, and $|\frown\rangle = (2)^{-1/2}(\hat{c}^\dagger_{1\uparrow}\hat{c}^\dagger_{2\downarrow} - \hat{c}^\dagger_{1\downarrow}\hat{c}^\dagger_{2\uparrow})|00\rangle$ is the singlet valence bond state. Higher energy electronic states can be safely neglected on the basis of the pump and probe pulses spectral regions used in Refs. [25,26].

The molecular coordinates are conveniently combined into an in-phase and an out-of-phase displacement $\hat{Q}_\pm = (2)^{-1/2}(\hat{Q}_1 \pm \hat{Q}_2)$. It is instructive to rewrite the model Hamiltonian in Eq. (4) for a dimer, using the symmetrized coordinates

$$\begin{aligned}\hat{H}_{\rm dim} = &-t\sum_{i,\sigma}(\hat{c}^\dagger_{i,\sigma}\hat{c}_{i+1,\sigma} + \text{H.c.}) + U_{\rm eff}\sum_i \hat{n}_{i,\uparrow}\hat{n}_{i,\downarrow} \\ &+ \frac{\hbar\omega_v}{4}(\hat{P}_+^2 + \hat{P}_-^2 + \hat{Q}_+^2 + \hat{Q}_-^2) \\ &+ \beta\frac{\hat{Q}_+^2 + \hat{Q}_-^2}{2}(\hat{n}_{1,\uparrow}\hat{n}_{1,\downarrow} + \hat{n}_{2,\uparrow}\hat{n}_{2,\downarrow}) \\ &+ \beta\hat{Q}_+\hat{Q}_-(\hat{n}_{1,\uparrow}\hat{n}_{1,\downarrow} - \hat{n}_{2,\uparrow}\hat{n}_{2,\downarrow}),\end{aligned} \tag{7}$$

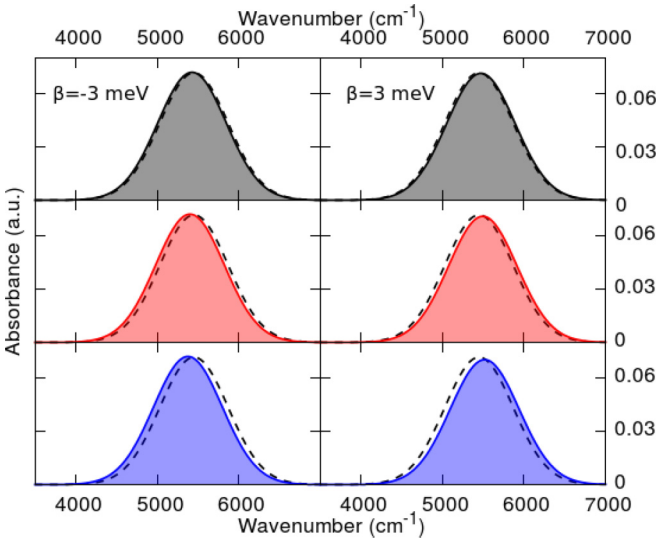

FIG. 2. Optical spectra in the CT region calculated for a dimer with $\omega_v = 1031$ cm^{-1} and $\beta = -3$ meV (left panels) and $+3$ meV (right panels). Panels from top to bottom show spectra calculated from the ground state and from $|v_1\rangle$ and $|v_2\rangle$ (see text). The dashed lines show the same spectra calculated for $\beta = 0$ (i.e., in the absence of vibrational coupling).

where $U_{\rm eff} = U - V$. Only $\hat{Q}_+$, the in-phase combination of molecular vibrations, is driven by the pump pulse. However we will perform a complete calculation, to verify the relevance to the problem of the coupling between the in-phase and out-of-phase combination of the modes, through their common coupling to the electronic system, as described by the last term in the above equation.

As discussed in different contexts [36,37], the non-adiabatic approach writes the Hamiltonian matrix on the basis obtained as the direct product of the three electronic states times the eigenstates of the harmonic oscillators associated with $\hat{Q}_+$ and $\hat{Q}_-$. The infinite basis associated with the harmonic oscillators are truncated to a large enough number of states as to ensure convergence (typically ten states are needed for each oscillator leading to a total dimension of 300). The eigenstates of the Hamiltonian matrix are the numerically exact non-adiabatic (vibronic) states describing the coupled electronic and vibrational motion and allow to calculate ground state properties as well as optical spectra.

We start our analysis discussing the effects of the pump pulse on the absorption spectrum. The pump beam is expected to populate the first few vibrational eigenstates associated with $\hat{Q}_+$. To identify the first vibrational eigenstate $|v_1\rangle$ among our non-adiabatic vibronic eigenstates, we select the $|E\rangle$ state having the largest transition dipole moment from the ground state, i.e., the largest $|\langle G|\hat{\mu}_{IR}|E\rangle|^2$, where $|G\rangle$ is the ground state. The second vibrational eigenstate $|v_2\rangle$ is obtained searching for the $|E\rangle$ state with the largest $|\langle v_1|\hat{\mu}_{IR}|E\rangle|^2$ matrix element, and so on. Figure 2 shows the optical spectra in the CT region, as probed by the probe-beam, calculated starting from $|G\rangle$, $|v_1\rangle$, and $|v_2\rangle$ states (top, middle, and lower panels, respectively), for a system with $\omega_v = 1031$ cm^{-1} and $\beta = -3$ meV (left panels) and $+3$ meV (right panels).

As expected, the pump beam in the mid-IR does not affect optical CT spectra in the absence of electron-vibration coupling ($\beta = 0$, dashed lines in Fig. 2). For negative β, left panels, a progressive red-shift of the absorption band is observed upon populating excited vibrational states, while a blue shift is observed for positive β. We expect that in the experimental conditions only $|v_1\rangle$ is appreciably populated. Indeed the direct transition probability from the ground to $|v_n\rangle$ states are negligible for $n > 1$, the only possibility to populate them being the excitation of excited states, a process that will lead to fast decreasing populations with increasing n. Results in left panel of Fig. 2, corresponding to model parameters relevant to mode 48, suggest, for realistic excitations to $|v_1\rangle$ and $|v_2\rangle$ states, a red-shift of $\sim$70 cm^{-1} of the CT band, in line with the experimental observation. We notice that with realistic model parameters and excitation schemes we cannot reproduce the appearance of the reflectivity peaks at $\sim$3000 cm^{-1} and $\sim$4000 cm^{-1}, as observed in Ref. [25]. Results reported in the Supplemental Material, [34] show that these features can only be reproduced by introducing an unphysically large β value, at least one order of magnitude larger than estimated through DFT. We underline that the excitation scheme we discuss is qualitatively different from that proposed in Ref. [25], where a pump-induced coherent population of the vibrational states of the electronic ground state is assumed. Indeed this kind of excitation is only possible via a more elaborate excitation scheme that implies a sequence of ultrafast (<30 fs) pulses in a pump and dump experiment [38–41].

To simulate the pump-probe spectra reported in Ref. [26] we explicitly introduce the pump-pulse in the Hamiltonian $\hat{H}(t) = \hat{H}_{\rm dim} - \hat{\mu}_{IR} F(t)$, where $F(t)$ is the t-dependent electric field associated with the mid-IR pump. Specifically, we consider a pump defined by a cosine at the frequency $\omega_{IR} = 1010$ cm^{-1} weighted by a Gaussian envelope with standard deviation $\sigma =$ 100 fs, as depicted in panel (a) of Fig. 3 [panel (b) shows the relevant Fourier transform]. The t-dependent Hamiltonian reads

$$\hat{H}(t) = \hat{H}_{\rm dim} - \sqrt{2}\eta F_0 \cos(\omega_{IR} t) e^{-\frac{t^2}{\sigma^2}} \hat{Q}_+, \qquad (8)$$

where F_0 is the amplitude of the applied field. The time-dependent Schrödinger equation for the coupled electronic and vibrational problem is solved through a numerical integration of the differential equation via a fourth-order Runge-Kutta approach (time step 0.1 fs) to obtain the time-dependent ground-state wave function as a linear combination of the non-adiabatic basis states.

The blue line in panel (c) of Fig. 3 shows the calculated expectation value of $\hat{Q}_+^2$. As expected, $\langle \hat{Q}_+^2 \rangle$ oscillates at twice the frequency of the driving pulse, as shown by the Fourier transform reported in panel (d). The antisymmetric $\hat{Q}_-$ coordinate, coupled to the driving field only through $\hat{Q}_+$, oscillates at the same frequency, but with an amplitude four orders of magnitude smaller than that observed for $\hat{Q}_+$, confirming that only the Brillouin zone-center modes are spectroscopically relevant.

Experimental spectra show damped oscillations, that suggest the need to account for some relaxation phenomena and hence for energy dissipation. To this effect, we introduce a bath of classical anharmonic oscillators coupled to the quantum

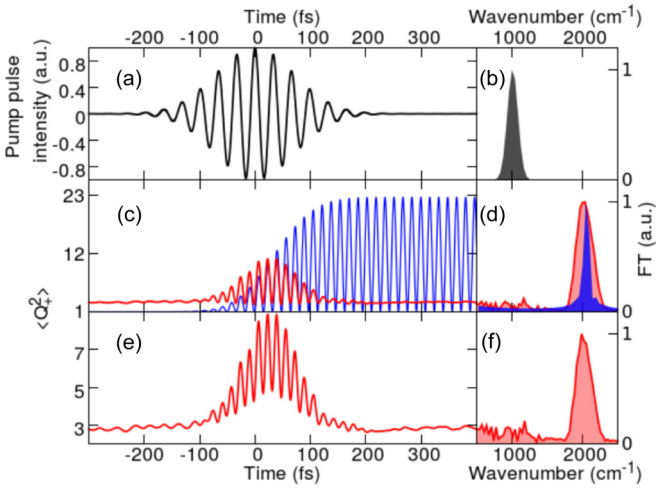

FIG. 3. Quantum dynamics of the coupled electron-vibrational system (same model parameters as in left panels of Fig. 2) driven by a mid-IR pulse. (a) and (b) Temporal evolution of the pulse and its Fourier transform, respectively. (c) and (d) Temporal evolution of $\langle \hat{Q}_+^2 \rangle$ calculated for a non-dissipative (blue line) and a dissipative (red line) driven system, and their Fourier transform, respectively. (e) and (f) Temporal evolution of $\langle \hat{Q}_+^2 \rangle$ calculated for a driven system with friction and accounting for the finite temporal resolution of the probe pulse (full width at half-maximum 10 fs) and its Fourier transform, respectively.

system [42,43]. In particular, we considered a linear chain of 20 classical particles [42] connected by anharmonic springs as described by the potential

$$V_b = \sum_{i=1}^{20} \left[\frac{\hbar\omega_b}{4} (q_i - q_{i+1})^2 + V_0 \chi^4 (q_i - q_{i+1})^4 \right], \qquad (9)$$

where q_i is the dimensionless coordinate of the i-th classical particle and we used fixed boundary conditions introducing an extracoordinate $q_{21}(t) = 0$. While the last oscillator (number 20) is connected to a fixed site, we connect the first oscillator of the linear chain to the quantum system, as follows:

$$\hat{H}_{s-b} = -\alpha \hat{Q}_+ q_1. \qquad (10)$$

To introduce dissipation, we account for a friction coefficient γ in the equation of motion relevant to the five particles at the end of the chain ($i =$ 16–20) and account for finite temperature introducing the Langevin random force, $R(t) = 2\xi\sqrt{\omega_b \gamma k_B T/\hbar\Delta t}$, where ξ is a Gaussian random variable of unit width and zero mean. The equation of motion for the classical particles then reads

$$\frac{\hbar}{2\omega_b}\frac{d^2 q_i}{dt^2} = -\frac{\partial V_b}{\partial q_i} + \delta_{i,1}\alpha\hat{Q}_+ + \frac{\hbar}{2\omega_b}\left(-\gamma\frac{dq_i}{dt} + R(t)\right)\delta_{i,j}, \qquad (11)$$

where $\delta_{i,1}$ ensures that only the first oscillator is coupled to the quantum coordinate $\hat{Q}_+$, while the dissipative terms in the round brackets only enter for oscillators number $j =$ 16–20. The α term in the above equation mixes the quantum and classical systems. The coupled quantum-classical dynamics is

calculated evolving the quantum system as described above for the non-dissipative case, adding the contribution from Eq. (10) for the q_1 value as relevant to each time step. Concomitantly, the classical equations of motion in Eq. (11) are numerically integrated (Verlet algorithm [44,45]) substituting the operator $\hat{Q}_+$ in Eq. (11) with its expectation value. The time step $\Delta t = 0.1$ fs is used for both quantum and classical calculations. In the following we will show results obtained averaging over several (typically 741) trajectories. An animation is provided in the Supplemental Material [34] showing the temporal evolution of $\langle \hat{Q}_+ \rangle$ and of the displacement of each classical oscillator.

The dissipation model is phenomenological and relevant parameters are set as to reproduce the experimental decay. The chain of classical oscillators has to be long enough (20 being the typical number [42]) as to avoid the direct cross-talk between the quantum system and the heat reservoir. The coupling between the quantum coordinate and the classical system, measured by α, has to be carefully balanced with the anharmonicity χ to enable a fast flow of energy away from the quantum sub-system, and with the friction coefficient γ in order to reach the correct canonical equilibrium state [42]. In particular, the red curve in Fig. 3 c is obtained for $\alpha = 0.16$ eV, $\chi = 4.4$, $\gamma = 10^{15}$ s^{-1}, $\omega_b = 60$ cm^{-1}, and $V_0 = 1$ eV at a working temperature $T = 298$ K. We stress that other choices are for sure possible to account for dissipation, but the specific choice of the parameters defining the dissipative systems are irrelevant, as long as a similar decay of the quantum coordinate is described.

The $\langle \hat{Q}_+^2 \rangle$ evolution in Fig. 3 c compares well with the oscillating behavior of the measured reflectivity shown in Ref. [26]. The agreement is further improved accounting for the finite temporal resolution of the experiment. Panel (e) of Fig. 3 shows the same curve, convoluted with a gaussian signal with full width at half-maximum of 10 fs (as to mimic the temporal profile of the probe pulse). The resulting curve compares very well with the experimental oscillations of the reflectivity that were previously simulated [26] imposing an ad hoc shape for the $U(t)$ curve obtained through a fitting procedure of the optical conductivity.

We are now in the position to calculate the temporal evolution of CT spectra, by diagonalizing the electronic Hamiltonian for each $\langle \hat{Q}_+(t) \rangle$ and evaluating relevant spectra. Results are shown in Fig. 4. Coherent oscillations of the CT band are clearly visible both in the color map (top panel) and in the time-section (bottom panel). The Fourier transform of the oscillating signal obtained from the time-section peaks at $\sim$2000 cm^{-1} as shown in the inset. These results compares favorably with experimental data reported in Fig. 4(b) of Ref. [26].

IV. THE SEMI-CLASSICAL APPROACH

The non-adiabatic calculation described above is computationally intensive and it is important to validate the quality of results obtained in the adiabatic approximation. We take advantage of the previous observation of the minor role played by the Q_- coordinate neglecting its coupling to the electronic

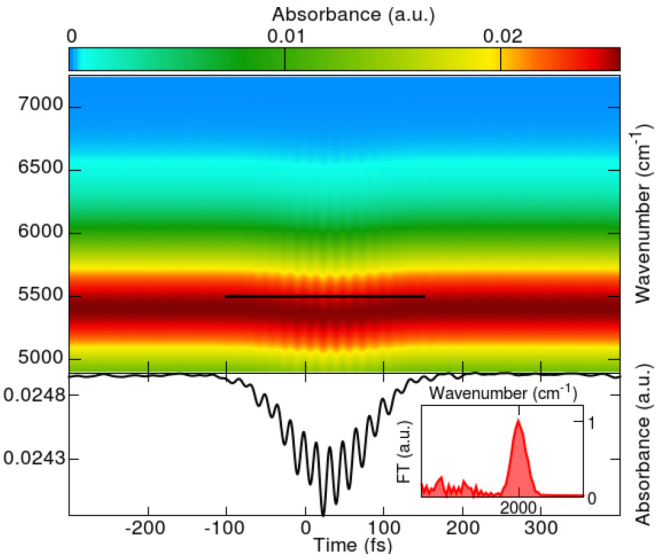

FIG. 4. Time evolution of the optical spectrum in the CT region obtained for a dissipative dimer with $\omega_v = 1031$ cm^{-1} and $\beta = -3$ meV, using a probe pulse with full width at half-maximum of 10 fs. Bottom panel shows section at $\omega = 5500$ cm^{-1} and relevant Fourier transform is reported in the inset. Average done over 741 trajectories.

system and write the adiabatic dimer Hamiltonian as follows:

$$\hat{H}_{ad} = \hat{H}_{el} + \frac{\hbar\omega}{4} Q_+^2 + \beta \frac{Q_+^2}{2} (\hat{n}_{1,\uparrow}\hat{n}_{1,\downarrow} + \hat{n}_{2,\uparrow}\hat{n}_{2,\downarrow}). \quad (12)$$

The above adiabatic Hamiltonian is obtained neglecting the vibrational kinetic energy and, apart from the harmonic vibrational potential, it describes a Hubbard Hamiltonian with a $U_{\text{eff}}(Q_+) = U - V + \beta Q_+^2/2$. The analytical solution for the Hubbard dimer leads to the Q_+ dependent ground state energy

$$E_{\text{g.s.}}(Q_+) = \frac{1}{2}\left(U_{\text{eff}}(Q_+) - \sqrt{U_{\text{eff}}^2(Q_+) + 16t^2} \right) + \frac{\hbar\omega}{4} \hat{Q}_+^2 \quad (13)$$

and the Q_+ dependent excitation energy and the squared transition dipole moment

$$\omega_{CT}(Q_+) = \frac{1}{2}\left(U_{\text{eff}}(Q_+) + \sqrt{U_{\text{eff}}^2(Q_+) + 16t^2} \right),$$
$$\mu_{CT}^2(Q_+) = \frac{1}{2}\left(1 - \frac{U_{\text{eff}}(Q_+)}{\sqrt{U_{\text{eff}}^2(Q_+) + 16t^2}} \right), \quad (14)$$

where the (dimensionless) dipole moment is measured in units with $ea = 1$, where a is the intermolecular distance. The three quantities are reported in Fig. 5.

The ground state energy as a function of Q_+, in the bottom panel of Fig. 5, represents the potential energy for the Q_+ motion. Accordingly, the classical dynamics of Q_+ driven by the pump pulse can be calculated by integrating the equation of motion:

$$\frac{d^2 Q_+}{dt^2} = \frac{\omega}{\hbar}\left(-\frac{\partial E_{\text{g.s.}}}{\partial Q_+} + F(t) \right) - \gamma \frac{dQ_+}{dt}, \quad (15)$$

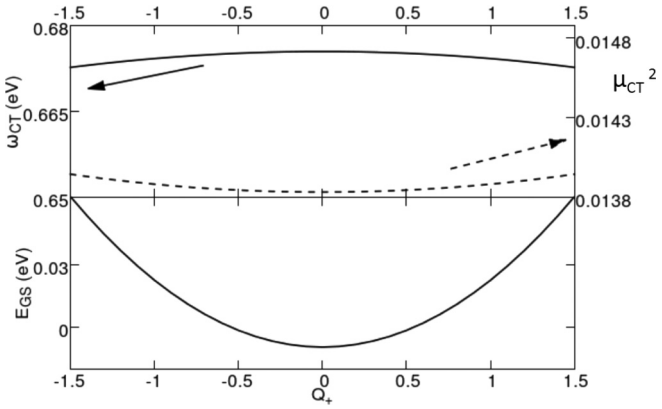

FIG. 5. The Hubbard dimer: the ground state energy (bottom panel), the transition frequency and the squared transition dipole moment (top panel) vs Q_+.

where the dynamics starts with the system $Q_+(t=0)=0$ and γ, the friction coefficient is set equal to 10^{15} s^{-1}, accounting for the finite vibrational excitation lifetime.

Results from the classical dynamics are reported in Figs. 6 and 7, for the same model parameters adopted previously. The $Q_+^2(t)$ evolution in Fig. 6 compares well with the non-adiabatic result. The spectral evolution in Fig. 7 is very similar to the non-adiabatic result, confirming the validity of the adiabatic approximation.

V. DISCUSSION

A model is presented to analyze a recent pump-probe experiment on ET-F_2TCNQ crystal [25,26]. The model is solved for the shortest lattice fragment, a $(ET^+)_2$ dimer. This choice allowed us to explore adiabatic and non-adiabatic solution of the problem, reaching similar results. Indeed within the adiabatic approach larger systems with up to 14 sites can be dealt with, but the dimer model represents a reliable approximation to describe the experiment, in view of the extremely localized nature of the ET-F_2TCNQ system, with a $U_{\rm eff} > 16t$.

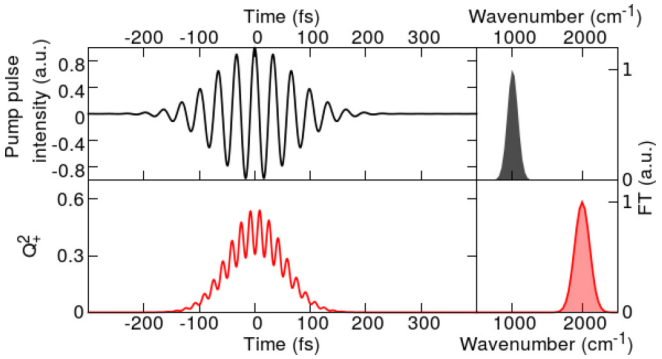

FIG. 6. Classical nuclear dynamics as induced by the pump pulse (upper left panel) on the ground state potential energy curve of the ET dimer. $Q_+^2(t)$, convoluted with the probe pulse profile (full width at half-maximum 10 fs), is shown in the bottom left panel. Corresponding Fourier transforms are reported in the right panels.

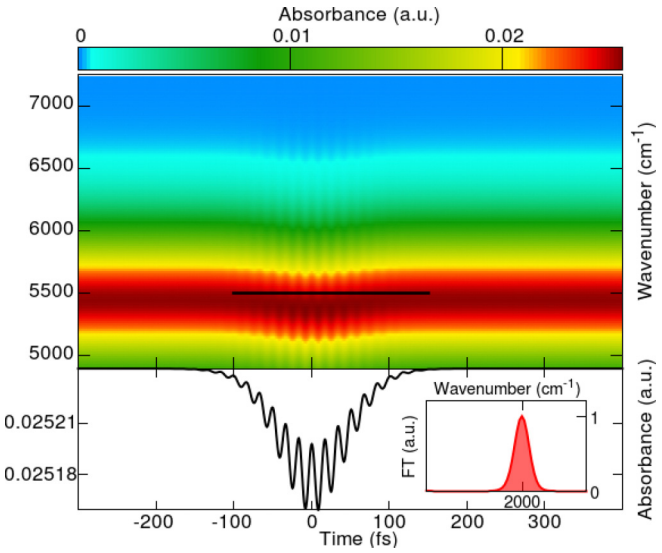

FIG. 7. Time evolution of the optical spectrum at 0 K, in the CT frequency region, calculated in the adiabatic approximation for the same model parameters as in Fig. 4, and $\gamma = 10^{15}$ s^{-1}. A section of the map at $\omega = 5500$ cm^{-1} is reported in the bottom panel, with relevant Fourier transform shown in the inset.

To validate this view, we carried out real-space diagonalization of the Hamiltonian in Eq. (1) for rings with up to 14 sites, setting $U = 0.666$ eV and $V = 0$. Relevant results are shown in Fig. 8. Following Resta, [46,47] we define the complex quantity

$$Z = \langle\psi|\exp\left(i\frac{2\pi\hat{\mu}_a}{N}\right)|\psi\rangle \tag{16}$$

with $|\psi\rangle$ representing the ground state wave function, i the imaginary unit, and $\hat{\mu}_a$ the dipole moment operator of the regular open-boundary chain defined in Eq. (5). The inverse modulus of Z measures the wave function delocalization and

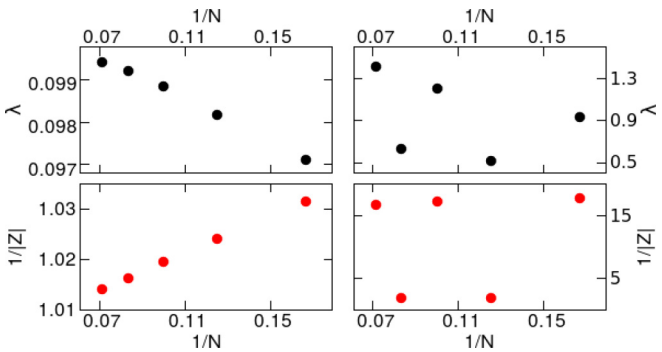

FIG. 8. The delocalization of the ground state wave function for the model in Eq. 1, with $V = 0$. Top panels, λ, the wave function delocalization length. Bottom panels, the inverse modulus of Z, as defined in the text. All quantities are reported vs the inverse number of sites. Left panels show results for $t = 0.04$ eV and $U = 0.666$ eV, as relevant to our system, right panels show results for a system with the same U, but a much larger $t = 1.1$ eV. In the right panels important finite size effects and delocalization are seen in terms of a large difference between $N = 4n$ and $N = 4n + 2$ systems.

is expected to converge to 1 in the thermodynamic limit for localized systems. This is clearly the case for our model with $t = 0.04$ eV (left panels of Fig. 8), while finite size effects are too large for $t = 1.1$ eV (right panels) to show convergence. Similarly, the dimensionless delocalization length, defined according to Resta [46,47] as $\lambda = \sqrt{-N \log |Z|^2}/(2\pi n_0)$ with n_0 being the electron average site density, amounts to a small fraction of the unit cell in our model, fully supporting our analysis based on a dimer model.

In conclusion, the THz pump and probe experiment described in Refs. [25,26] can be described accounting for the quadratic modulation of the Hubbard U by ET^+ vibrations, as proposed in the original papers. However, in the original works, spectra were reproduced imposing an ad hoc temporal dependence of the Hubbard U. Here we adopt a model Hamiltonian parametrized against quantum chemical calculations and propose a rigorous calculation of the dynamics of the quantum system driven by the THz pulse. To quantitatively reproduce the temporal evolution of experimental spectra, the model has to be extended to explicitly account for energy dissipation, a non-trivial task bringing us in the realm of open quantum systems. In this respect, a phenomenological approach was adopted connecting the quantum system to an array of classical anharmonic oscillators connected in turn to a heat reservoir. Overall our effort demonstrates that pump-probe experiments can be rigorously addressed studying the dynamical behavior of driven open quantum systems.

ACKNOWLEDGMENTS

This work was supported by Italian MIUR through PRIN2012T9XHH7_002 and by CINECA through IsC43_MMM-CT and IsC50_MMM-time.

[1] J. B. Torrance, Acc. Chem. Res. **12**, 79 (1979).
[2] D. Jérome, Chem. Rev. **104**, 5565 (2004).
[3] G. Saito and Y. Yukihiro Yoshida, Bull. Chem. Soc. Jpn. **80**, 1 (2007).
[4] E. Dagotto, Science **309**, 257 (2005).
[5] B. J. Powell and R. H. McKenzie, Rep. Prog. Phys. **74**, 056501 (2011).
[6] R. K. S. Horiuchi, Y. Okimoto and Y. Tokura, Science **299**, 229 (2003).
[7] F. Kagawa, S. Horiuchi, and Y. Tokura, Crystals **7**, 106 (2017).
[8] G. D'Avino, A. Painelli, and Z. Soos, Crystals **7**, 177 (2017).
[9] A. Girlando, A. Painelli, S. A. Bewick, and Z. G. Soos, Synth. Metals **141**, 129 (2004).
[10] S. Tomic and M. Dressel, Rep. Prog. Phys. **78**, 096501 (2015).
[11] M. Masino, N. Castagnetti, and A. Girlando, Crystals **7**, 108 (2017).
[12] C. Giannetti, M. Capone, D. Fausti, M. Fabrizio, F. Parmigiani, and D. Mihailovic, Adv. Phys. **65**, 58 (2016).
[13] S. D. Silverstri, G. Cerullo, and G. Lanzani, *Coherent Vibrational Dynamics* (CRC Press, Boca Raton, FL, 2008).
[14] J. Chesnoy and A. Mokhtari, Phys. Rev. A **38**, 3566 (1988).
[15] H. Fragnito, J.-Y. Bigot, P. Becker, and C. Shank, Chem. Phys. Lett. **160**, 101 (1989).
[16] H. Uemura and H. Okamoto, Phys. Rev. Lett. **105**, 258302 (2010).
[17] T. Miyamoto, H. Uemura, and H. Okamoto, J. Phys. Soc. Jpn. **81**, 073703 (2012).
[18] L. Cavatorta, A. Painelli, and Z. G. Soos, Phys. Rev. B **91**, 174301 (2015).
[19] B. Green, S. Kovalev, V. Asgekar, G. Geloni, U. Lehnert, T. Golz, M. Kuntzsch, C. Bauer, J. Hauser, J. Voigtlaender, B. Wustmann, I. Koesterke, M. Schwarz, M. Freitag, A. Arnold, J. Teichert, M. Justus, W. Seidel, C. Ilgner, N. Awari, D. Nicoletti, S. Kaiser, Y. Laplace, S. Rajasekaran, L. Zhang *et al.*, Sci. Rep. **6**, 22256 (2016).
[20] G. Cerullo and S. D. Silvestri, Rev. Sci. Instrum. **74**, 1 (2003).
[21] S.-H. Shim, D. B. Strasfeld, E. C. Fulmer, and M. T. Zanni, Opt. Lett. **31**, 838 (2006).
[22] S.-H. Shim, D. B. Strasfeld, and M. T. Zanni, Opt. Express **14**, 13120 (2006).
[23] T. Miyamoto, H. Yada, H. Yamakawa, and H. Okamoto, Nat. Commun. **4**, 2586 (2013).
[24] T. Morimoto, T. Miyamoto, and H. Okamoto, Crystals **7**, 132 (2017).
[25] S. Kaiser, S. R. Clark, D. Nicoletti, G. Cotugno, R. I. Tobey, N. Dean, S. Lupi, H. Okamoto, T. Hasegawa, D. Jaksch, and A. Cavalleri, Sci. Rep. **4**, 3823 (2014).
[26] R. Singla, G. Cotugno, S. Kaiser, M. Först, M. Mitrano, H. Y. Liu, A. Cartella, C. Manzoni, H. Okamoto, T. Hasegawa, S. R. Clark, D. Jaksch, and A. Cavalleri, Phys. Rev. Lett. **115**, 187401 (2015).
[27] T. Hasegawa, S. Kagoshima, T. Mochida, S. Sugiura, and Y. Iwasa, Solid State Commun. **103**, 489 (1997).
[28] H.-L. Liu, L.-K. Chou, K. A. Abboud, B. H. Ward, G. E. Fanucci, G. E. Granroth, E. Canadell, M. W. Meisel, D. R. Talham, and D. B. Tanner, Chem. Mater. **9**, 1865 (1997).
[29] S. Wall, D. Brida, S. R. Clark, H. P. Ehrke, D. Jaksch, A. Ardavan, S. Bonora, H. Uemura, Y. Takahashi, T. Hasegawa, H. Okamoto, G. Cerullo, and A. Cavalleri, Nat. Phys. **7**, 114 (2011).
[30] A. Girlando, L. Grisanti, M. Masino, I. Bilotti, A. Brillante, R. G. Della Valle, and E. Venuti, Phys. Rev. B **82**, 035208 (2010).
[31] E. Scriven and B. J. Powell, J. Chem. Phys. **130**, 104508 (2009).
[32] M. J. Frisch, G. W. Trucks, H. B. Schlegel, G. E. Scuseria, M. A. Robb, J. R. Cheeseman, G. Scalmani, V. Barone, B. Mennucci, G. A. Petersson, H. Nakatsuji, M. Caricato, X. Li, H. P. Hratchian, A. F. Izmaylov, J. Bloino, G. Zheng, J. L. Sonnenberg, M. Hada, M. Ehara *et al.*, *Gaussian 09* (Gaussian, Inc., Wallingford CT, 2009), http://gaussian.com/glossary/g09/.
[33] A. Fortunelli and A. Painelli, Phys. Rev. B **55**, 16088 (1997).
[34] See Supplemental Material at http://link.aps.org/supplemental/10.1103/PhysRevB.96.075106 for a full list of U, V electron-nuclear quadratic coupling constants, and relative IR intensities calculated through DFT. A video of a simulation is also provided.
[35] A. Girlando, J. Phys. Chem. C **115**, 19371 (2011).
[36] G.-P. Borghi, A. Girlando, A. Painelli, and J. Voit, Europhys. Lett. **34**, 127 (1996).

[37] L. Del Freo, F. Terenziani, and A. Painelli, J. Chem. Phys. **116**, 755 (2002).
[38] D. J. Tannor and S. A. Rice, J. Chem. Phys. **83**, 5013 (1985).
[39] D. J. Tannor, R. Kosloff, and S. A. Rice, J. Chem. Phys. **85**, 5805 (1986).
[40] S. A. Rice, D. J. Tannor, and R. Kosloff, J. Chem. Soc., Faraday Trans. 2 **82**, 2423 (1986).
[41] M. Shapiro and P. Brumer, J. Chem. Soc., Faraday Trans. **93**, 1263 (1997).
[42] P. V. Parandekar and J. C. Tully, J. Chem. Phys. **122**, 094102 (2005).
[43] C. P. van der Vegte, A. G. Dijkstra, J. Knoester, and T. L. C. Jansen, J. Phys. Chem. A **117**, 5970 (2013).
[44] L. Verlet, Phys. Rev. **159**, 98 (1967).
[45] N. Gronbech-Jensen and O. Farago, Mol. Phys. **111**, 983 (2013).
[46] R. Resta and S. Sorella, Phys. Rev. Lett. **82**, 370 (1999).
[47] R. Resta, J. Phys.: Condens. Matter **14**, R625 (2002).